Nanoscale

Accepted Manuscript

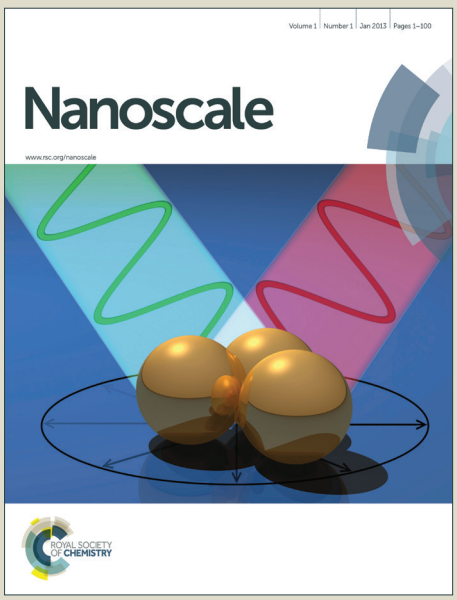

ROYAL SOCIETY OF CHEMISTRY

www.rsc.org/nanoscale

Journal Name

RSCPublishing

ARTICLE

Engineering of nanoscale defect patterns in CeO_2 nanorods via *ex-situ* and *in-situ* annealing

Cite this: DOI: 10.1039/xoxxoooooox

Tamil Selvan Sakthivel[a], David L. Reid[a], Umananda M. Bhatta[b†], Günter Möbus[b], Dean Christopher Sayle[c] and Sudipta Seal[a*]

Received ooth January 2012,
Accepted ooth January 2012

DOI: 10.1039/xoxxoooooox

www.rsc.org/

Single-crystalline ceria nanorods were fabricated using a hydrothermal process and annealed at 325 °C - 800 °C. As-synthesized CeO_2 nanorods contain a high concentration of defects, such as oxygen vacancies and high lattice strain. Annealing resulted in improved lattice crystalline quality along with evolution of novel cavity-shaped defects in the nanorods with polyhedral morphologies and bounded by e.g. {111} and {100} (internal) surfaces, confirmed for both air (ex-situ) and vacuum (in-situ) heating. We postulate that the cavities evolve via the agglomeration of vacancies within the as-synthesized nanorods.

Introduction:

Ceria (CeO_2) and its sub-oxides have been intensively studied for a long time due to their distinctive properties of oxygen storage capacity, oxygen ion conductivity, hardness, and reactivity[1-5]. CeO_2 has been used as an industrial catalyst for three-way catalysis (TWC) and fluid catalytic cracking (FCC) process[6-8]. Ceria can be used as a polishing agent in the microelectronic industry for the chemical mechanical planarization (CMP)[9, 10] and as an oxygen ion conductor in solid oxide fuel cells[11], amperometric oxygen monitors[12], and oxygen pumps[13]. Ceria also finds other uses as luminescence material[14], in gas sensors[15], sunscreen cosmetics[16], etc. Both experimental[17] and theoretical[18] studies proved that the physicochemical properties of CeO_2 materials exhibited surface structure dependent features. As we mentioned earlier[18] the (100) surface is integrally more responsive and catalytically significant as compared to the (110) and (111) surfaces, therefore, growth of controllable CeO_2 nanostructures with well-defined exposed surfaces is of significant importance.

This crystal structure and morphology play significant roles in numerous applications, which made researchers to concentrate on nanocrystalline CeO_2 preparation in recent years[19]. CeO_2 are exceptional oxygen buffers due to their redox capability[20]. Changes in cerium oxidation state will be accommodated via oxygen vacancies. The defect and valence structure of CeO_2 is active and may adjust impulsively or in response to physical restrictions such as oxygen partial pressure, temperature, and doping with other ions, as well as surface stresses[21-25]. Although there are a few reported attempts to explain the surface defects of CeO_2 nanoparticles after annealing of the samples[19, 26-30] to the best of our knowledge, the annealing effect on the structural and microstructural properties of the CeO_2 nanorods has not been reported in detail. Thus, it is valuable to investigate the effect of annealing of the CeO_2 nanorods.

Herein, we report on novel insight into the annealing induced defect engineering in ceria nanorods by concurrent observations of (i) defect and strain annihilation and (ii) formation of new defects, with the former involving point defects and being detectable by XRD while the latter appearing in TEM and involving larger cavities. In addition to the experimental investigation, atomic computer simulation was employed to help rationalize how a rich defect microstructure including isolated and associated cerium and oxygen vacancies, oxygen interstitials and grain-boundaries on CeO_2 nanorods.

Experimental Section

Materials Synthesis: The type and concentration of cerium salt directly influence the size and morphology of CeO_2 nanostructures. There are many reports explaining the effect of cerium precursors involving the combined effects of cerium ions (Ce^{3+} and Ce^{4+}) as well as associated counter-anions (SO_4^-, NO_3^-, OH^-, and Cl^-)[1,3,5,31]. In our preparation, only $Ce(NO_3)_3$ and NaOH are used as reactants and an essentially ligand-free self-assembly of ceria nanocrystals into nanorods is assumed via the oriented attachment mechanism. Single crystalline CeO_2 nanorods were synthesized by the procedure previously reported by the same group[32]. In detail, in a typical synthesis, 0.45 M of $Ce(NO_3)_3.6H_2O$ and an appropriate amount of NaOH (22.5 M) were dissolved in 20 ml of deionized water separately. These two solutions were mixed in a Teflon bottle, and stirred for 30 min with the formation of milky slurry. The resultant product was allowed to stand at 120 °C for 24 h in a stainless steel vessel autoclave, which led to crystallization under static hydrothermal conditions. The white precipitates were centrifuged, washed with

deionized water several times, and dried at 80 °C in air overnight. The as-synthesized solid product was annealed at 325 °C and 800 °C in oxidizing environment for 3 h.

Instruments and Characterization: The X-ray diffraction (XRD) patterns of as-synthesized and heated nanorods were obtained using a Rigaku D/MAX diffractometer and a Cu X-ray source. XRD specimens were prepared by placing the powders on a zero-background silicon (510) plate using a 0.5% solution of nitrocellulose in amyl acetate to adhere the specimen powder to the plate. Optical properties were studied using photoluminescence (PL), spectra (Hitachi F700) were recorded by dispersing ceria samples in water as dispersant using a concentration of 5 µM. The emission properties were measured by exciting the ceria samples at 370 nm. The XPS measurements were carried out in an ion-pumped chamber (evacuated to 2 x 10^{-9} torr) of a PE-PHI5400 spectrometer, employing $Mg_{K\alpha}$ radiation (BE = 1253.6 eV). The binding energy (BE) for the samples was calibrated by setting the measured BE of C 1s to 284.6 eV. The microstructure and defects of ceria samples were studied using high-resolution transmission electron microscopy (HRTEM) using a Philips Tecnai and a JEOL JEM R005 aberration corrected atomic resolution microscope, both operating at 300 kV, and a JEOL JEM2010F at 200kV. The *in-situ* heating experiments were conducted using a JEOL JEM 3010 microscope and a Gatan single tilt heating holder using CNP loaded carbon-Cu grids sandwiched between Ta washers inserted in a Ta specimen-boat.

Results and Discussion

Structural and optical characterization of CeO_2 nanorods: The crystallite size, lattice strain, lattice (im-) perfection and defect concentration, are the most important characteristics affecting the intensity and width of Bragg peaks in X-ray diffraction[33,34]. Figure 1A illustrates typical XRD patterns of as-synthesized and annealed CeO_2 nanorods. The XRD pattern of all CeO_2 nanorods shows a high intensity peak at $2\Theta = 28°$ and other minor peaks. All the diffraction peaks can be indexed to pure cubic phase (fluorite structure, JCPDS 34-0394 space group Fm-3m) of CeO_2. The sharpening of peaks with increasing annealing temperature is an expected standard behaviour for oxide ceramics, as annealing induces defect-healing, strain release, and grain growth. However, as reported below, TEM image footage indicates that all rod particles are single crystalline and do not change size or shape during annealing. That leaves defect and strain annihilation as the only causes for the peak sharpening. Williamson-Hall analysis (W-H) could be used to extract micro-strain by plotting the peak-broadening as a function of diffraction angle. However, the high anisotropy of the nanorods, and the preferential crystallographic growth-direction of the rods, causes different reflections to arise from a different diameter D in the sense of Scherrer's law, which influences the W-H extrapolation. Results of such analysis as reported in table 1, using a single average D-value, are therefore approximate and meant to report trends only.

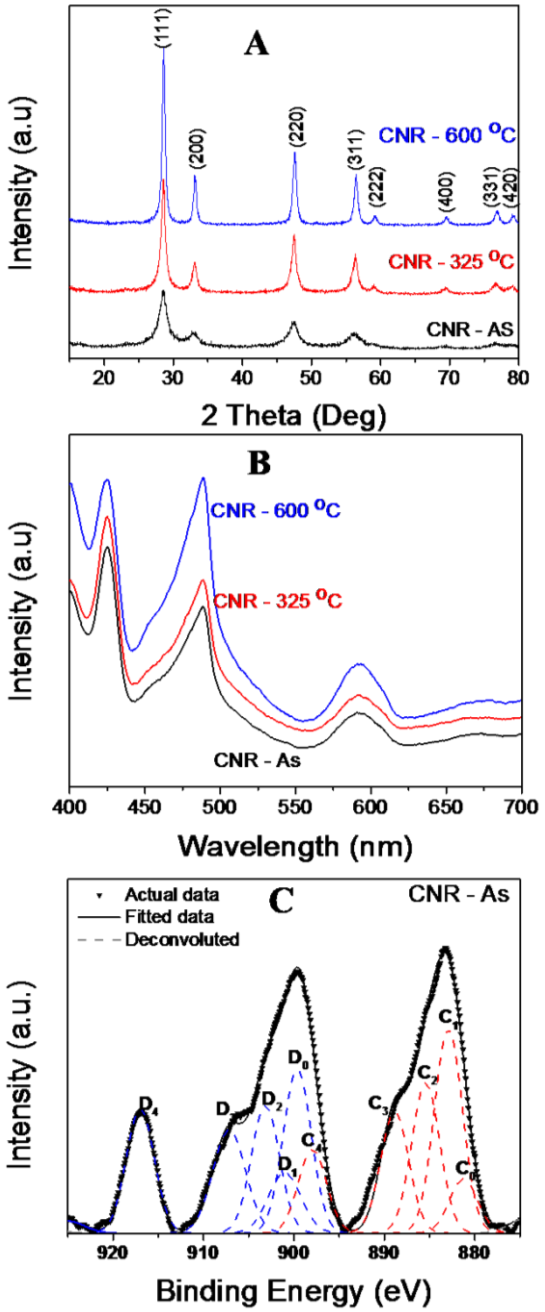

Figure 1: (A) Comparative XRD patterns of CeO2 nanorods (CNRs) without annealing ("AS") and annealed at different temperature (325, and 800 oC) in air. (B) PL spectra of CeO2 nanorods via excitation at 370 nm. (C) XPS Ce 3d spectra of as-synthesized CeO2 nanorods.

Lattice constants are determined for each of the sample and a correlation is established between lattice constants and lattice strain with the changes in the oxygen vacancy concentration. No change in crystallite size of the CNRs is found on moving from room temperature (RT) to 800 °C with the simultaneous decrease in the lattice constant and strain. The lattice expansion of as-synthesized ceria nanoobjects compared to bulk ceria is likely due to the presence of oxygen vacancies and Ce^{3+}, which both increase bond-distances[35-37]. These defects will particularly

cumulate near and on the surface. In the case of nanorods also internal defects arising from oriented attachment growth could contribute. The excess defects produce short-range stress fields which are, as a mean value, compressive in nature[36]. Annealing of as-synthesized CNRs in air at 325 °C and 800 °C progressively reduces the point defect concentration from these regions and decreases the lattice strain.

Table 1: Physicochemical properties of CeO_2 nanorods (Lattice constant (a), Crystallite size (D), and Lattice strain (ε), were estimated by W-H method from XRD data; Oxygen vacancy concentration from Lattice constant (a), and Ce^{3+} concentration from XPS)

Sample	XRD				XPS
	a (Å)	D (nm)	ε x10^{-3}	Oxy. Vacancy x10^{21}/cm^3	Ce^{3+} Concentration
CNR-As	5.4135	50.2	2.6900	5.926	0.39
CNR-325 °C	5.4131	49.8	1.9800	4.978	0.35
CNR-800 °C	5.4123	49.5	0.6725	3.081	0.32

Using Kröger-Vink notation[38,39] for oxygen vacancies, the following equation[35] applies which allows vacancy concentration and lattice constants to be interrelated:

$$\frac{\sqrt{3}}{4}(a' - a_0) = C\left[r_{ce^{3+}} - r_{ce^{4+}} + \frac{1}{4}\left(r_{V_o^{\cdot}} - r_{O^{2-}}\right)\right] \quad (1)$$

In this equation, $r_{V_o^{\cdot}}$ is the oxygen vacancy radius, $r_{ce^{3+}}$ is the Ce^{3+} radius, and 'a' is the lattice constant of our prepared CeO_2 nanorods. The lattice constant (a_o) of bulk CeO_2 is 5.4110 Å (JCPDS 34-0394). The sizes of the ions are $r_{ce^{3+}}$ = 0.1283 nm, $r_{ce^{4+}}$ = 0.1098 nm, $r_{O^{2-}}$ = 0.124 nm and $r_{V_o^{\cdot}}$ = 0.138 nm[39]. The lattice constants *a(T)* from our XRD data for CNR-As, CNR-300 °C, and CNR-800 °C are found to be 5.4135 Å, 5.4131 Å, and 5.4123 Å, respectively. The total concentration of oxygen vacancies in each sample is obtained after substituting the values of the aforementioned parameters in equation (1). The concentration of these vacancies decreases with annealing temperature. Decrease in the concentration of these vacancies decreases the magnitude of lattice strain and lattice constant.

As the PL spectrum is also associated to the defect levels in the CeO_2 nanorods, we studied the PL response of as-synthesized and annealed CeO_2 nanorods. In figure 1B, the position of different emission peaks are almost identical before and after annealing. The change in emission intensity is interrelated to the presence of multiple defects in the crystal structure such as interstitials and vacancies. High oxygen defect levels are present in the samples, and the visible light emission peaks are mostly related with oxygen vacancies with trapped electrons[40]. Previous studies, on PL of CeO_2, have ascribed the emission at ~425 nm to surface defects in CeO_2[41, 42]. In the PL spectra, it is seen that the emission intensity of CNR-As is lower than that of CNR-325 °C and CNR-800 °C. This infers that the high oxygen vacancy concentration acts as luminescence quencher in CNR-As[43]. At 800 °C, many of the non-radiative surface and bulk defects are removed. Decrease in point defect concentrations also increases the carrier mobility, enhancing the radiative carrier recombination process. Therefore, from the analysis of the PL spectra, we can say that reduction of the defect concentration is the prerequisite to get efficient visible light emissions, as observed in CNR-800 °C.

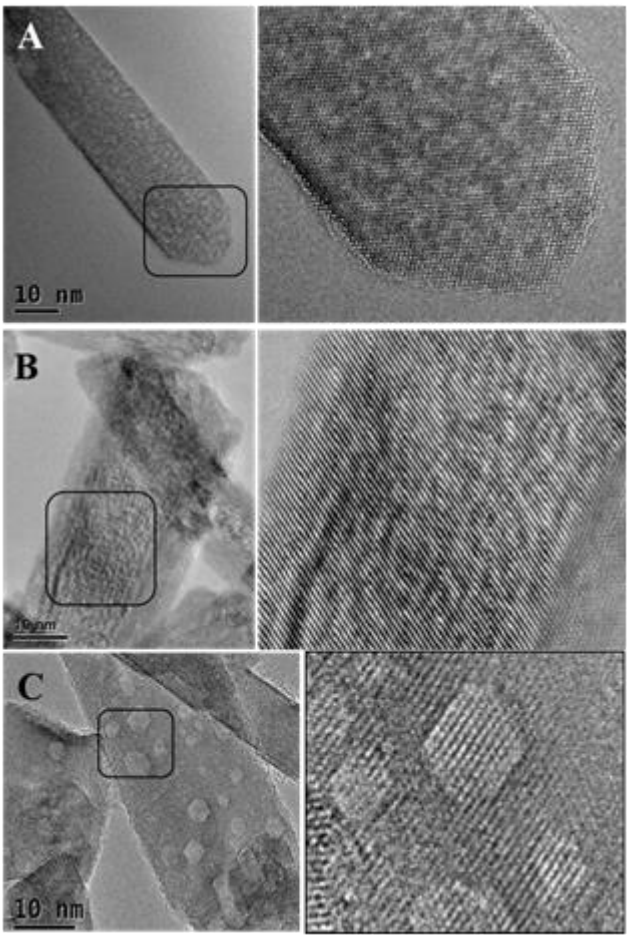

Figure 2: *Ex-Situ* annealing: HRTEM images, showing various amounts of imperfect crystallinity (image pairs with zoom-in of black rectangles): **(A)** as-synthesized CeO_2 nanorod. Rod-direction <110>. **(B)** Sample annealed at 325 °C in air. **(C)** Annealed at 800 °C: The rod-direction for (B,C) is <211>. The viewing directions for (A-C) are of <110> type. (JEOLJEM 3100-R005 @300kV)

The detailed X-ray photoelectron spectroscopy (XPS) study for CeO_2 nanorods is presented in figure 1C. XPS spectra of heated nanorods are shown in figure S1. Ten peaks are deemed necessary to model these spectra, which are labeled as C_0, C_1, C_2, C_3, C_4, D_0, D_1, D_2, D_3, D_4. According to the literature,[31, 35-37] the peaks labeled C0, C1, C2, C3 and C4 refer to 3 $d_{3/2}$ states, while the peaks labeled as D_0, D_1, D_2, D_3 and D_4 refer to 3 $d_{5/2}$ states. The peaks characteristic of Ce^{3+} states are labeled as C_0, C_2, D_0, and D_2; while remaining peaks are attributed to Ce^{4+} ions. The peak spots of all CNRs are listed in Table S1. A semi-quantitative investigation of the combined peak area can offer the concentration of Ce^{3+} ions in the as-synthesized and annealed nanorods. It can be calculated as[35,36].

$$[Ce^{3+}] = \frac{A_{C_0} + A_{C_2} + A_{D_0} + A_{D_2}}{\sum A_i} \quad (2)$$

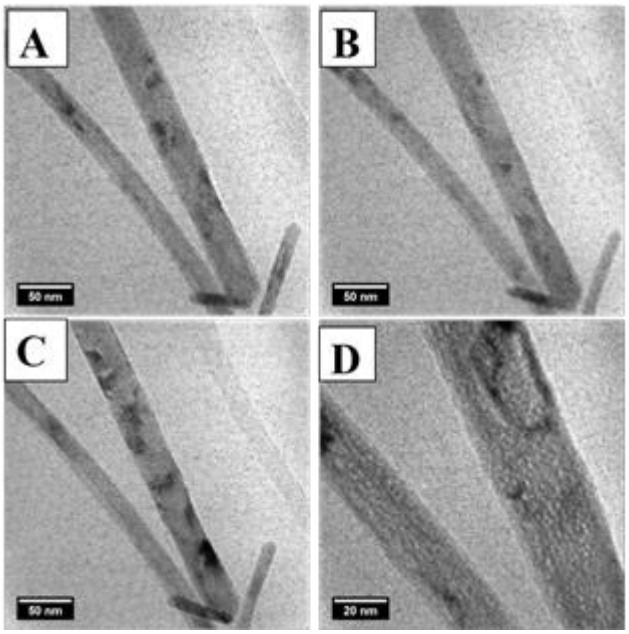

Figure 3: In-situ annealing: TEM images of CeO_2 nanorods mounted in heating holder. **(A)** at room temperature, **(B)** 80 minutes in-situ heated at 325 °C, **(C+D)** 80 min annealed at 600 °C, and cooled down to RT, and then again 180 min annealed at 600 °C (totally 80 + 180 minutes, the experiment was done over two days) (JEOL JEM 3010 @300kV).

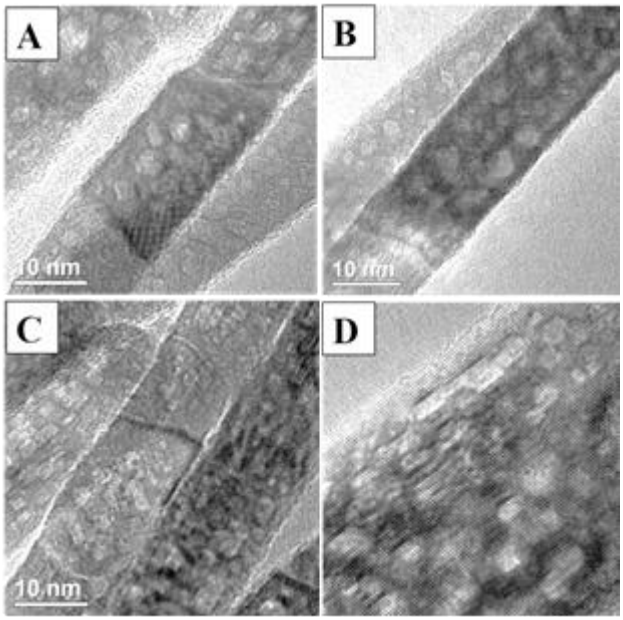

Figure 4: Details of patches due to projected cavities found through in-situ heating in HRTEM in various rods, imaged at room temperature following in-situ heating at 600 °C. (JEOLJEM 2010F @200kV). (a) Patches of mainly "projected octahedral" shape forming in central grain areas, away from surface and grain boundaries. (b) Rod with facetted and more roundish patches at the back and more rectangular shape at front. (c) Group of nanorods in another place with variety of patch shape including roundish, rectangular and oval shape. (d) Another rod (zoom-in) with patches of a more rectangular projected shape and preferred texture along the rod-axis direction.

where A_i is the combined area of peak "i". The ratios of Ce^{3+} are listed in table 1. It shows that the Ce^{3+} ion concentration decreases with increase in annealing temperature. The larger ratio of Ce^{3+} ions increases the lattice strain and consequently increments the lattice parameter. The correlation between the XRD and XPS results confirms that Ce^{3+} ion concentration is in proportion to the lattice parameter increment.

Electron microscopy characterization of CeO_2 nanorods: At first, imaging by TEM is performed (Figure 2) at room temperature for nanorods with *ex-situ* annealing (at 325 and 800 °C) and without *ex-situ* annealing, before we present *in-situ* annealing in Figures (3-4). Nanorods typically range 5 to 20 nm in lateral size and beyond 200 nm in longitudinal size. Most rods are single-crystalline (Figures 2-3), although grains and boundaries can also occasionally be found (Figure 4). The rod surfaces are mostly smooth and the tip of the rod can show a variety of shapes, including faceted tip-shape (Figure 2A), rectangular end (Figure 2B) or of apparent rounded shape (Figure S2), which turns out in detail to be micro-faceting of sub-1 nm length facets of mostly {111} type. The non-annealed nanorod of Figure 2A is characterized by a fine-speckled fluctuation of brightness superimposed to its single-crystalline (seemingly perfect) lattice-fringe pattern. The speckle is non-ordered, of about 2 nm size, and has no sharply delimited facets. Such a pattern is characteristic of internal local strain distributions, e.g. due to point defects or small vacancy clusters, which lead to fluctuating Bragg diffraction and varying HRTEM background intensity, supporting the X-ray diffraction line broadening of Figure 1. It is also possible that the speckle pattern and strain fluctuation indicates residual fingerprints of the history of nanorod-growth via the principle of "Oriented Attachment" (OA)[44]. During OA, adjacent nanoparticles from the aqueous solution are assembled together by distributing a mutual crystallographic arrangement followed by connecting these particles at a planar boundary to convert towards nanorods, finally leading to the single crystalline anisotropic structure growth. Generally, the driving force for this natural OA is to decrease the overall surface energy by removing the surfaces at which the crystallites join. Specifically for fcc-type minerals, two types of OA pathways could occur, either aligned along the [211] direction with exposed {111} surfaces or the attachment is along the [110] direction with exposed {200} surfaces. The prior would be more promising because the CeO_2 {111} surface is the most stable surface[44]. In this work examples of both rod directions are found, such as [211] in Figures 2B-C, and Figure S2, and [110] in Figure 2A.

Results of the *ex-situ* annealing at 325 °C in oxidizing environment are presented as Figure 2B, represented here by a different rod, which shows less smooth surfaces than in Figure 2A, while at the same time the internal strain-related speckle appears here more of a strain-band pattern (see bottom-left of Figure 2B). After heating at 800 °C, the previous random speckle patterns appear to be less pronounced. Instead, a new type of bright patches appears, which now are about 2-5 nm in diameter and there are different shapes of these 3D defects, mostly facetted in an identical way as known from HRTEM images of CeO_2 nanoparticles, enclosed mainly by {111} and {100}-cap surfaces. It was previously reported that annealing in argon and nitrogen did not change the morphology of CeO_2 nanorods even

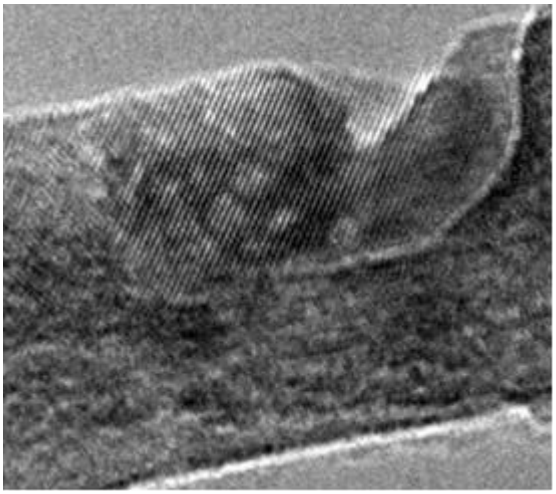

Figure 5: Formation of octahedral-projected patches in area of high-intensity electron beam irradiation (FEGTEM JEOL 2010F @ 200kV), along with general thinning and ablation, without any heating applied.

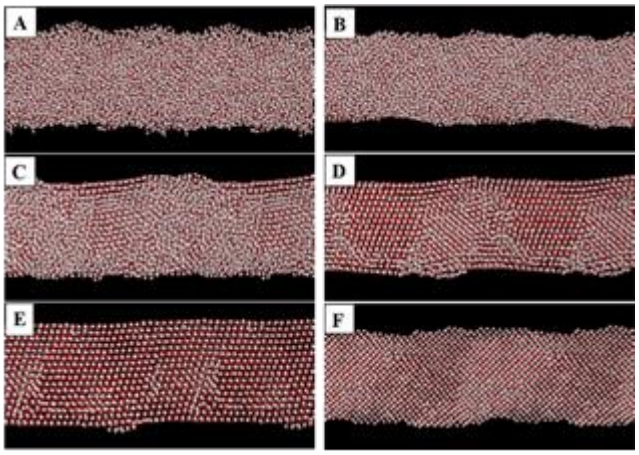

Figure 6: Simulated crystallization of a ceria nanorod. Oxygen atom positions are represented by the small red spheres and Cerium atom positions are represented by the large white spheres.

at very high temperature (900 °C)[45] while the annealing in air at 800 °C caused some surface damage and thinning of nanorods[46]. In contrary, other reported that no significant change in morphology and no visible damage to CeO_2 nanorods were spotted after annealing in air upto 800 °C[47]. In our experiment, annealing in oxidizing environment upto 800 °C caused no change in morphology but changes the internal strain state and leads to formation of new facet-type defect patches (see Figure 2C).

***In-situ* TEM experiments of CeO_2 nanorods:** Above annealing experiments have been repeated under high vacuum, typical for TEM, using a TEM heating holder. Temperatures of similar to the ex-situ settings as reported above have been applied, except for using 600 °C instead of 800 °C (reported in-situ temperatures are approximate thermocouple readings of the heating holder, which could deviate from exact sample temperature depending on thermal conductivity of the sample). Our finding is that vacuum heating can reproduce most of the heating patterns, especially the formation of bright facetted patches. This effect is therefore independent of the oxidizing environment used during annealing. Annealing with constant exposure to an electron beam would rather resemble a reducing environment, as oxygen loss precedes cerium loss during irradiation. Figure 3 shows the *in-situ* TEM images for room temperature (Figure 3A), followed by 80 minutes annealing at 325 °C (3B), and 180 minutes at 600 °C in addition to the previous annealing (3C), which consisted of 80 min annealing at 600 °C, cooling down to RT, and then again increased to 600 °C for 180 minutes, totally 80+180 minutes., Figure 3D shows a magnified version of 3c. No significant changes in size, morphology and surface smoothness were found. However, Figure 3d reveals some development of speckle and bright patchy patterns, which is found for various rods, some more imaged in Figure S3. After cooling back to room temperature, without exposing to air, these new patches were imaged at even higher magnification in Figure 4: The correspondence to the patches found from air heating is obvious. Some greater variety of patch shape (believed to be 3D defects in projection) including roundish, rectangular and oval indicates that possibly some metastable defects are frozen in, while air heating favored projected facetted octahedral-type patches.

Interpretation of the heating patterns: The origin of the bright patches as a projection of 3D defects is evidenced by some general observations:

(i) Brightness is always lower than for the crystal matrix, indicating loss of projected mass-density in beam direction, being aware that mass-thickness contrast is only a coarse and first approximation in phase-contrast HRTEM images, governed by complex electron wave interference processes. The contrast jump between patches and matrix is too strong to be caused by just one monolayer of missing material (as evident from HRTEM image simulation thickness series in[48]).

(ii) Most patches are enclosed by straight lines, and some conform to a perfect projected capped octahedron which is corresponding to the well-known octahedral facets (e.g. {111}, {100}). This feature resembles the concept of "inverted" ceria nanoparticles inside nanorods, now appearing as nano-voids. The orientation of these 3D defects matches also the orientation of transient nanoparticles during oriented attachment formation theory of rods[49].

(iii) The patches do not correspond to perforated material, as lattice fringes are seen inside patches. These fringes continue un-shifted from the surrounding HRTEM lattice and prove that the defects are superimposed to continuous layers of single crystal above and/or below the defect in beam direction.

(iv) The patches appear in plan-view in projection, and are not seen (bar one exception) in cross-section as indents or surface pits on the sides of nanorods and also the patches are located within the inner 3/4 or 4/5 of the rod diameter and never reach to the final 5 monolayers of the side-faces of rods.

Cumulated evidence supports the patches as projections of fully facetted 3D cavities, rather than 2D surface features, which

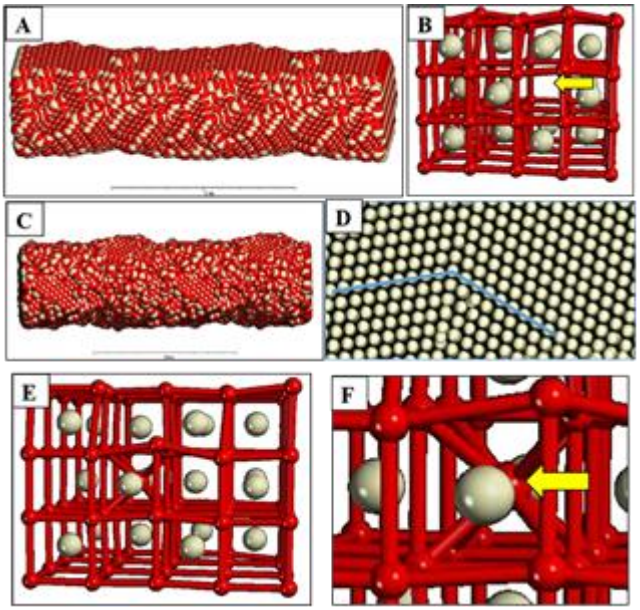

Figure 7: Atomistic models of ceria nanorods and their defect microstructures. (A) Ceria nanorod with [211] growth direction. (B) Segment of (A) depicting a cerium vacancy as indicated by the yellow arrow. (C) Ceria nanorod, which comprises a grain-boundary that traverses the nanorod. (D) Atomistic structure of the grain-boundary (oxygen ions are not shown). (E) Atomistic structure of an oxygen interstitial. (F) Enlarged segment of (E); the arrow shows the position of the oxygen interstitial. Cerium atom positions are represented by the white spheres and oxygen ions are represented by the red spheres.

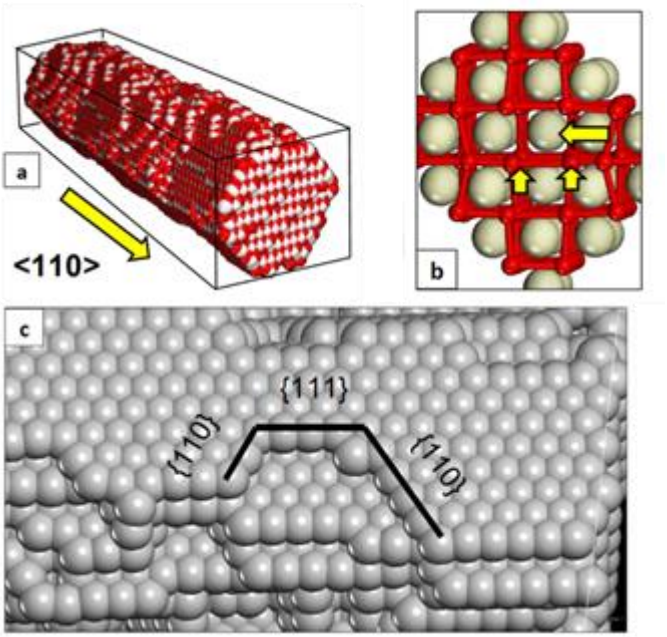

Figure 8: Atomistic structure of model ceria nanorods **(a)** perspective view of the nanorod showing the [110] growth direction and hexagonal nanorod cross-section **(b)** segment of (a) showing a defect cluster comprising one Ce vacancy and two oxygen vacancies as indicated by the yellow arrows. **(c)** Enlarged section of the surface of the nanorod (a) showing the steps, edges and corners and close packing of the cerium ions (oxygen ions are not shown).

minimize their internal surface energy in equivalence to the externals surfaces of nanoparticles. Accumulation of vacancies into regular facetted large clusters of reduced material would produce similar HRTEM patterns, however, the striking similarity of our heating patterns with published patches from irradiation damage[50], identified as voids, favors the first interpretation. For comparison, we attach an example of such electron irradiation induced projected octahedral-facetted patches from ceria nanorods in Figure 5. For this experiment the electron beam had been temporarily focused to the region outlined by a fringe, while for all other experiments (Figures 2-4) the electron beam was spread to more than the field of view, and did not generate irradiation-induced patterns. Beyond oxygen migration, oxygen-loss due to bulk-heating has recently been established via conductivity measurements in $BaTiO_3$[51], and due to much higher RT O mobility, the O migration in CeO_2 could start at lower temperatures.

Computer Modeling and Atomic Simulation: Atomistic computer simulation was used to help support and complement our experimental findings. In particular, full atomistic models of ceria nanorods were generated using molecular dynamics (MD) simulation using pair potentials[51]. The atomistic models of the nanorods were generated by simulating their crystallization from amorphous precursors; procedures have been documented previously[53]. Simulating the crystallization enables the hierarchical structural complexity of the model nanorods to evolve within the atomistic models including: polymorphic crystal structure, microstructure (point defects, dislocations, grain-boundaries) and nanostructure (growth direction, morphology and surfaces exposed). Here we characterize structurally three model nanorods: (a) nanorod with a growth direction along [211], (b) nanorod with growth direction along [110] and (c) nanorod that comprises a grain-boundary.

The nanorods were analyzed using molecular graphical techniques using VMD[53] and Materials Studio. The simulated crystallization of the nanorod with growth direction along [211] is shown in figure 6. Initially, the nanorod is amorphous, figure 6(a) and at a particular time a crystalline seed spontaneously evolves within the amorphous sea of ions, figure 6(b,c). This seed then nucleates the crystallization of the whole nanorod, figure 6(d,e) together with the evolution of a rich microstructure including isolated and associated point defects, grain-boundaries 6(d)), nanorod morphology and surfaces exposed. Under extended simulated annealing, the grain-boundary is annealed out, figure 6(f), and some of the point defects move to energetically more favorable positions.

Analysis of the atomistic models reveal that the nanorods are highly defective, figure 7, 8. In particular, we observe many isolated oxygen and cerium vacancies, figure 7(b), oxygen interstitials, figure 7(e,f) and vacancy clusters, such as a single cerium vacancy associated with two neighboring oxygen vacancies, figure 8(b). We also observe much larger defect clusters comprising several oxygen and cerium vacancies (not shown); such complex vacancy clusters are perhaps better described as voids within the nanorod. Analysis using molecular graphics revealed that the defects evolve during the crystallization process. In particular, as ions condense onto the surface of the nucleating seed, they locate at lattice positions. However, not all lattice positions become filled and a vacancy is

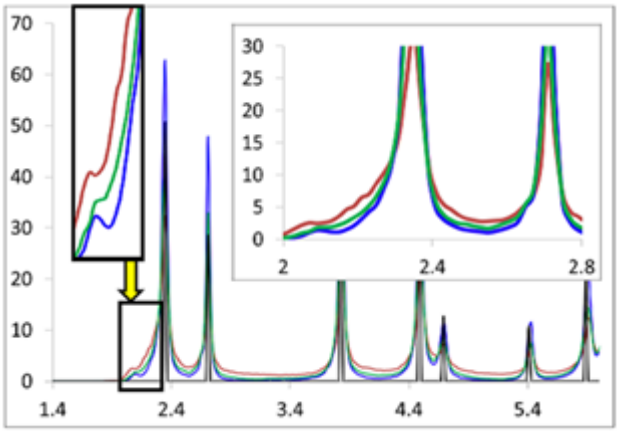

Figure 9: Radial distribution function (RDF) calculated for the three nanorods showing the considerable deviation of the Ce-O bond distances from those found in the bulk parent material; the RDF of bulk ceria is shown to compare. Abscissa: Ce-O interatomic separation (Å); ordinate: g(r). Red trace: nanorod with grain-boundary; green trace: nanorod with growth direction along [110]; blue trace: nanorod with growth direction along [211]; black trace: parent bulk material.

created when other ('amorphous') ions condense around this unfilled lattice position. Ions can also locate, during the simulated crystallization process, at 'non-fluorite' lattice positions as evidenced by the oxygen interstitial in figure 7(e,f). Inspection of figure 8(c) shows a 'pit' on the surface of the ceria nanorod that has a pseudo-hexagonal profile similar to those observed in our experiments, figure 2(c). In particular, during the simulated crystallization/high temperature annealing, Ce and O ions are mobile and move across the surface to facilitate close packing of the Ce sublattice; the steps/edges that evolve conform to (energetically stable) {111} and {110} surfaces. Steps, edges and corners of the model nanorods exhibit similar structural features, figure 7(a,c), figure 8(a). Accordingly, we postulate that the as-synthesized nanorod, figure 2(a), comprises a high concentration of vacancies, which, under annealing conditions agglomerate to facilitate nanocavities with stable (internal) surfaces such as {111}, {110} and {100}. Oxygen ion mobility is vacancy driven and cerium ions move along the cavity surfaces of the nanorod– analogous (energy-driven) to cerium ions moving on the nanorod surface as shown by our simulations; previously we observed (experimentally) the mobility of cerium ions on a CeO_2 (100) surface[56]. We note that ceria nanorods with pores[55] and titania nanorods with dense nanocavities[57,58] have been synthesized by others

Experimentally, we found that the lattice parameters of the nanorods are different compared to the parent bulk material, with lattice strains of up to 0.5%. To gauge the strain within the model nanorods, Ce-O Radial Distribution Functions (RDF) were calculated, fig 9. The RDF traces reveal significant deviation from Ce-O distances in the parent bulk material indicating significant strain within the lattice that extends to the 'bulk' regions of the nanorods. We note that the nanorod that comprises a grain-boundary suffers the most strain. In particular, the strain emanates from both the relaxation of surface ions and the relaxation of ions within the core-region of the grain-boundary. Careful inspection of the first Ce-O peak (2.4 Å), reveals a small shoulder at about 2.1Å, as indicated by the yellow arrow in figure 9. This peak corresponds to the ionic relaxation of Ce and O ions around a point defect such as a vacancy. The size of this peak is therefore indicative of the defect concentration within the model nanorods.

Conclusion

In summary, we can say that oxygen vacancies are playing the key role in the tuning of the structural and microstructural properties of CeO_2 nanorods via annealing. Two types of oxygen-related defects are found: Initially, disordered small oxygen defects (0D - point-defects or small vacancy clusters) increase the lattice strain and broaden diffraction peaks significantly, while a small lattice expansion is found for such as-synthesized CeO_2 nanorods. On thermal treatment the small oxygen defects are gradually healed and replaced through oxygen migration by a second type of oxygen defect through evolution of nanocavities with polyhedral morphologies within the nanorods. The first type of defect is strongly detectible via XRD but barely visible in HRTEM, while the second type is prominent in HRTEM and undetectable in XRD.

MD simulation was used to simulate the crystallization of ceria nanorods from amorphous precursors. The atomistic models derived comprised a high concentration of defects including Ce and O vacancies and vacancy clusters, O interstitials and grain-boundaries; calculated Radial Distribution Functions was used to quantify the defect concentration. We postulate that the nanocavities evolve within the nanorods via the agglomeration of the vacancies within the defective (as-prepared) nanorods.

Previous work[59,60] have found some defect-contrast features in ceria nanostructures by TEM, however, patches were dark and of very small size while roundish and of random distribution. In contrast, our new TEM findings show bright extended patches of sharp delimitation organized along crystallographic orientations with facets commensurate with those commonly found for nanoparticles of ceria. These cavities are formed from internal atomic and vacancy diffusion, not involving air-born oxygen, as they appear for both air heating and vacuum heating. They are mostly internal cavities and not surface-pores. All together our annealing experiments prove that systematic heat treatments provide a further experimental route of ceria surface activity tuning apart from previously proposed tuning via doping, irradiation, and shape tuning during synthesis, and can be combined with any of these other routes.

Acknowledgements

This work was made possible through grants from NSF NIRT for Nanoceria research (NSF International supplement: CBET 1028996), and EPSRC, UK, Nos EP/H001220, EP/H001298.

Notes and references

[a]Advanced Materials Processing and Analysis Center (AMPAC), NanoScience Technology Center (NSTC), Materials Science

Engineering (MSE). University of Central Florida 4000, Central Florida Boulevard, Orlando, Fl 32816, USA. E-mail: Sudipta.Seal@ucf.edu
[b]Department of Materials Science and Engineering, University of Sheffield, Mappin Street, Sheffield S1 3JD, UK.
[c]School of Physical Science, University of Kent, Canterbury, Kent, CT2 7NZ, UK .
Author present address
†Umananda M. Bhatta
Jain University, Centre for Emerging Technologies\Jain Global Campus
Jakkasandra-562 112, Kanakapura Tq, Ramanagaram Dist,
Karnataka, India

†Electronic Supplementary Information (ESI) available: [W-H analysis result, XPS spectrum of annealed CeO_2 nanorods, XPS binding energies of individual peak, additional HRTEM images of as-synthesized CeO_2 nanorods, and in-situ TEM images in various places after heating.]. See DOI: 10.1039/b000000x/

1 D. S. Zhang, C. S. Pan, L. Y. Shi, J. H. Fang, *Eur. J. Inorg. Chem.*, 2008, **15,** 2429-2436.
2. T. X. Sayle, B. J. Inkson, A. Karakoti, A. Kumar, M. Molinari, G. Möbus, S. C. Parker, S. Seal and D. C. Sayle, *Nanoscale*, 2011, **3**, 1823-1837.
3. Q. Wu, F. Zhang, P. Xiao, H. Tao, X. Wang, Z. Hu and Y. Lü, *J. Phys. Chem. C*, 2008, **112**, 17076-17080.
4. Y. Xia, P. Yang, Y. Sun, Y. Wu, B. Mayers, B. Gates, Y. Yin, F. Kim and H. Yan, *Adv. Mater.*, 2003, **15**, 353-389.
5. H. X. Mai, L. D. Sun, Y. W. Zhang, R. Si, W. Feng, H. P. Zhang, H. C. Liu and C. H. Yan, *J. Phys. Chem. B*, 2005, **109**, 24380-24385.
6. A. Trovarelli, C. de Leitenburg, M. Boaro, and G. Dolcetti, *Catal. Today*, 1999, ***50***, 353-367.
7. A. Trovarelli. *Catal. Rev. Sci. Eng.*, 1996, **38**, 439-520.
8. J. Kašpar, P. Fornasiero, and M. Graziani, *Catal. Today*, 1999, **50**, 285-298.
9. Y. Lee, Y.-J. Seo and H. Jeong, *Electron. Mater. Lett.*, 2012, **8**, 523-528.
10. C. A. Coutinho, S. R. Mudhivarthi, A. Kumar and V. K. Gupta, *Appl. Surf. Sci.*, 2008, **255**, 3090-3096.
11. C. T. Campbell and C. H. Peden, *Science*, 2005, **309**, 713-714.
12. T. Yu, J. Joo, Y. I. Park and T. Hyeon, *Angew. Chem.*, 2005, **117**, 7577-7580.
13. G. A. Deluga, J. R. Salge, L. D. Schmidt and X. E. Verykios, *Science*, 2004, **303**, 993-997.
14. A. Corma, P. Atienzar, H. Garcia and J.-Y. Chane-Ching, *Nature materials*, 2004, **3**, 394-397.
15. N. Izu, S. Nishizaki, W. Shin, T. Itoh, M. Nishibori and I. Matsubara, *Sensors*, 2009, **9**, 8884-8895.
16. L. De Marzi, A. Monaco, J. De Lapuente, D. Ramos, M. Borras, M. Di Gioacchino, S. Santucci and A. Poma, *Int. J. Mol. Sci*, 2013, **14**, 3065-3077.
17. S. C. Kuiry, S. D. Patil, S. Deshpande and S. Seal, *J. Phys. Chem. B*, 2005, **109**, 6936-6939.
18. T. X. T. Sayle, M. Cantoni, U. M. Bhatta, S. C. Parker, S. R. Hall, G. Möbus, M. Molinari, D. Reid, S. Seal and D. C. Sayle, *Chem. Mater.*, 2012, **24**, 1811-1821.
19. C. Sun, H. Li and L. Chen, *Energy Environ. Sci.*, 2012, **5**, 8475-8505.
20. J. Chen, S. Patil, S. Seal and J. F. McGinnis, *Nature Nanotechnology*, 2006, **1**, 142-150.
21. G. Herman, *Surf. Sci.*, 1999, **437**, 207-214.
22. F. Lu, F. Meng, L. Wang, Y. Sang and J. Luo, *Micro & Nano Letters*, 2012, **7**, 624-627.
23. E. Mamontov, T. Egami, R. Brezny, M. Koranne and S. Tyagi, *J. Phys. Chem. B*, 2000, **104**, 11110-11116.
24. B. W. Sheldon and V. B. Shenoy, *Phys. Rev. Lett.*, 2011, **106**, 216104.
25. Y. F. Chen, Z. Wang, Q. Wang, B. Yin and G. L. Shen, *Key Eng. Mater.*, 2010, **434**, 850-852.
26. Z. Wang, S. Seal, S. Patil, C. Zha and Q. Xue, *J. Phys. Chem. C*, **111**, 11756-11759.
27. K. I. Fukui, Y. Namai and Y. Iwasawa, *Appl. Surf. Sci.*, 2002, **188**, 252-256.
28. O. Stetsovych, J. Beran, F. Dvorák, K. Masek, J. Myslivecek and V. Matolín, *Appl. Surf. Sci.*, 2013, **285P**, 766–771.
29. A.G. El Hachimi, H. Zaari, M. Boujnah, A. Benyoussef, M. El Yadari and A. El Kenz, *Computational Materials Science*, 2014, **85**, 134-137.
30. S. Yamazaki, T. Matsui, T. Ohashi, and Y. Arita, *Solid State Ionics*, 2000, **136,** 913-920.
31. M. Hirano and E. Kato, *J. Am. Ceram. Soc.*, 1996, **79**, 777-780.
32. T. Sakthivel, S. Das, A. Kumar, D. L. Reid, A. Gupta, D. C. Sayle and S. Seal, *ChemPlusChem*, 2013, **78**, 1446-1455.
33. J.-M. Zhang, Y. Zhang, K.-W. Xu and V. Ji, *Solid State Commun*, 2006, **139**, 87-91.
34. N. S. Ramgir, Y. K. Hwang, I. S. Mulla and J.-S. Chang, *Solid State sciences*, 2006, **8**, 359-362.
35. S. Deshpande, S. Patil, S. V. Kuchibhatla and S. Seal, *Appl. Phys. Lett.*, 2005, **87**, 133113.
36. Q. Xu, W. Lei, X. Li, X. Qi, X., J. Yu, G. Liu, J. Wang and P. Zhang, *Environ. Sci. Technol.*, 2014, **48,** 9702−9708.
37. P. Dutta, S. Pal, M. Seehra, Y. Shi, E. Eyring and R. Ernst, *Chem. Mater.*, 2006, **18**, 5144-5146.
38. M. Nolan, J. E. Fearon and G. W. Watson, *Solid State Ionics*, 2006, **177**, 3069-3074.
39. X. Zhou and W. Huebner, *Appl. Phys. Lett.*, 2001, **79**, 3512-3514.
40. B. Choudhury and A. Choudhury, *Mater. Chem. Phys.*, 2012, **131**, 666-671.
41. S. Phoka, P. Laokul, E. Swatsitang, V. Promarak, S. Seraphin and S. Maensiri, *Mater. Chem. Phys.*, 2009, **115**, 423-428.
42. S. Gnanam and V. Rajendran, *J Sol-Gel Sci Technol*, 2011, **58**, 62-69.
43. A. Kumar, S. Babu, A. S. Karakoti, A. Schulte and S. Seal, *Langmuir*, 2009, **25**, 10998-11007.
44. N. Du, H. Zhang, B. Chen, X. Ma and D. Yang, *J. Phys. Chem. C*, 2007, **111**, 12677-12680.
45. T. Zhai, X. Fang, M. Liao, X. Xu, H. Zeng, B. Yoshio and D. Golberg, *Sensors*, 2009, **9**, 6504-6529.
46. R. L. Penn and J. F. Banfield, *Science*, 1998, **281**, 969-971.
47. K.-S. Lin and S. Chowdhury, *Int. J. Mol. Sci*, 2010, **11**, 3226-3251.
48. U. M. Bhatta, I. M. Ross, T. X. Sayle, D. C. Sayle, S. C. Parker, D. Reid, S. Seal, A. Kumar and G. Möbus, *ACS nano*, 2012, **6**, 421-430.
49. Y. Du, M. Yashima, T. Koura, M. Kakihana and M. Yoshimura, *Scripta Metallurgica et Materialia*, 1994, **31**, 327-332.
50. W. Xu, Y. Zhang, G. Cheng, W. Jian, P. Millett, C. Koch, S. Mathaudhu and Y. Zhu, *Mater. Res. Lett.*, 2014, 1-8.
51. H. Beltrán, E. Cordoncillo, P. Escribano, D. C. Sinclair and A. R. West, *J. Appl. Phys.*, 2005, **98**, -.

52. D. C. Sayle, X. Feng, Y. Ding, Z. L. Wang and T. X. T. Sayle, *J. Am. Chem. Soc.*, 2007, **129**, 7924-7935.
53. T. X. T. Sayle, M. Molinari, S. Das, U. M. Bhatta, G. Mobus, S. C. Parker, S. Seal and D. C. Sayle, *Nanoscale*, 2013, **5**, 6063-6073.
54. W. Humphrey, A. Dalke and K. Schulten, *J. Mol. Graphics*, 1996, **14**, 33-38.
55. G. Möbus, Z. Saghi, D. C. Sayle, U. M. Bhatta, A. Stringfellow and T. X. T. Sayle, *Adv. Funct. Mater.*, 2011, **21**, 1971-1976.
56. I. Florea, C. Feral-Martin, J. Majimel, D. Ihiawakrim, C. Hirlimann and O. Ersen, *Cryst. Growth Des*, 2013, **13**, 1110-1121.
57. W. Q. Han, L. J. Wu, R. F. Klie and Y. M. Zhu, *Adv. Mater.*, 2007, **19,** 2525-2529.
58. H. Zhu, J. Tao and X. Dong, *J. Phys. Chem. C*, 2010, **114,** 2873-2879.
59. N. J. Lawrence, J. R. Brewer, L. Wang, T.-S. Wu, J. Wells-Kingsbury, M. M. Ihrig, G. Wang, Y.-L. Soo, W.-N. Mei and C. L. Cheung, *Nano Lett.*, 2011, **11**, 2666-2671.
60. X. Liu, K. Zhou, L. Wang, B. Wang and Y. Li, *J. Am. Chem. Soc.*, 2009, **131**, 3140-3141.

Table of Contents, Graphic

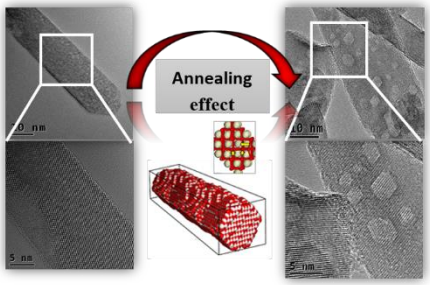

Annealing of cerium oxide nanorods results in the evolution of distinct cavities with polyhedral morphologies due to the high temperature activated rearrangement of cerium and oxygen atoms and vacancies on the as-synthesized nanorods.